
# Study of Smith-Purcell Radiation

Mémoire de Master
présenté par

**Vitalii Khodnevych**

Stage effectué au
Laboratoire de l'Accélérateur Linéaire
Université Paris-Sud

sous la direction de
Nicolas Delerue

Master 2 Grands Instruments
Université Paris-Sud

Août 2017
Orsay

## Annotation

Beam diagnostics are extremely important for accelerators, especially plasma accelerators. Smith-Purcell radiation can be used as a non destructive, ultrahigh resolution technique for longitudinal beam profile measurements.

During this internship we obtained first results of beam profile measurements at the CLIO accelerator. Electron pulses of few picosecond length, high charge and the 45 MeV Linac make CLIO the ideal location to test advanced longitudinal profile diagnostics. We designed and manufactured electronics and software for data acquisition and analysis. In result, we measure the spectrum and reconstruct the bunch profile for wide region of buncher and section phase, buncher power. For future upgrades of the setup we design and made experimental test of THz mesh filters for signal filtering.

In parallel we made polarization measurements of Smith-Purcell radiation at SPESO experiment. SPESO is an experiment at Synchrotron SOLEIL to study the Coherent Smith-Purcell radiation. In 2016, as part of upgrade, polarizer was installed. We analyze the date since September 2016 and made a map of polarization.

Intermediate results of this work was presented at International particle accelerator conference 2017 ([1], [2]).

# Contents

# Chapter 1

# Introduction

In last 75 years, particle accelerators became an important tools for basic research, medicine, life sciences etc. Now from accelerators are required compact size, high energy, small and short bunches. This requirements can satisfy laser plasma accelerators. They could be used in wide range of application: from high-energy colliders to free-electron lasers. The primary limitations of these accelerators include their shot-to-shot stability and the fine-tuning of the beam parameters. A crucial step that precedes the ability to fine-tune and stabilize the electron beam parameters, however, is the ability to measure them. As a result, a significant focus of plasma accelerators research has been dedicated to the development of diagnostic techniques. They require ultahigh temporal resolution methods of non-destructive beam diagnostics [3].

There is presented one of the future beam diagnostics: Smith-Purcell technique. It's non-destructive technique, which is able measure bunches up to femtosecond range [4], so it completely satisfies the conditions as one of diagnostic techniques for plasma accelerators. Work on this tool will consist from two parts: experimental study of physical properties of Smith-Purcell radiation (Polarization, spatial distribution, etc.) and creation of prototype of longitudinal beam profile monitor based on this effect. We report on first results achieved with this prototype and discuss possible ways to upgrade it. Also we describe polarization measurements and results of SPESO experiment at SOLEIL.

# Chapter 2

# Smith-Purcell experiment at CLIO

We report on measurements of Coherent Smith-Purcell radiation (SPR) at the CLIO Free Electron Laser. We describe experimental setup and methods with which we extract the data. At the first stage of our analysis we will try to prove the presence of SPR and will try check basic properties of it. At second stage will try to extract data from this spectrums and reconstruct profiles. Results are presented as functions of accelerator parameters (cavity & buncher phase, buncher power).

## 2.1 Smith-Purcell radiation

In 1953 Smith and Purcell observe that when "electron passes close to the surface of a metal diffraction grating, moving at right angles to the rulings, the periodic motion of the charge induced at the surface of the grating should give rise to radiation" [5]. An intuitive model for the Smith- Purcell effect is the emission of radiation by the periodically vibrating dipole moment of the electron and its image charge [6].

So, Smith-Purcell radiation (SPR) occurs when a charged particle move above a metallic periodic structure. Emitted radiation is spread in solid angle. The wavelength of the radiation for SPR depends on the observation angle $\Theta$ in polar plane according to the following formula:

$$\lambda = \frac{l}{n}(\frac{1}{\beta} - cos\Theta) \tag{2.1}$$

where l is the grating period , n is the order of radiation and $\beta$ is the relativistic velocity.

For one electron the emission spectrum (single electron yield [7]) is given by:

$$\frac{d^2 I_1}{d\omega d\Omega} = \frac{e^2\omega^2 l^2}{4\pi^2 c^3} R^2 exp(-2x_0/\lambda_e) \tag{2.2}$$

where $\omega$ is the emission frequency, $d\Omega$ is the solid angle, e is the electron charge, c is the speed of light, $R^2$ is the "grating efficiency factor", $x_0$ is the beam-grating separation

(BGS) and $\lambda_e$ is the evanescent wavelength:

$$\lambda_e = \lambda \frac{\beta\gamma}{2\pi\sqrt{1+(\beta\gamma\sin\Theta\sin\phi)^2}} \tag{2.3}$$

where $\beta, \gamma$ are the relativistic parameters of the particles in the beam, $\phi$ – azimuthal observation angle (counts from perpendicular to the base of grating surface). The total spectrum is proportional to the single electron yield and contains incoherent ($\sim N$) and coherent ($\sim N^2$) components:

$$\frac{d^2I}{d\omega d\Theta} = \frac{d^2I_1}{d\omega d\Theta}[N + N(N-1)F(\omega)] \tag{2.4}$$

where N is the number of electrons in the bunch and $F(\omega)$ is the form factor of the longitudinal (time) profile of the bunch. Using the phase recovery methods, such as Kramers-Kronig or Hilbert [8], it is possible to recover the phase and then the time profile of the bunch.

So Smith-Purcell radiation can be used to monitor the longitudinal beam profile.

## 2.2 CLIO accelerator

The CLIO free electron laser is an accelerator built in 1991. It is described in details in [9] and it is shown on figure 2.1. The CLIO accelerator consist of a thermionic gun, a

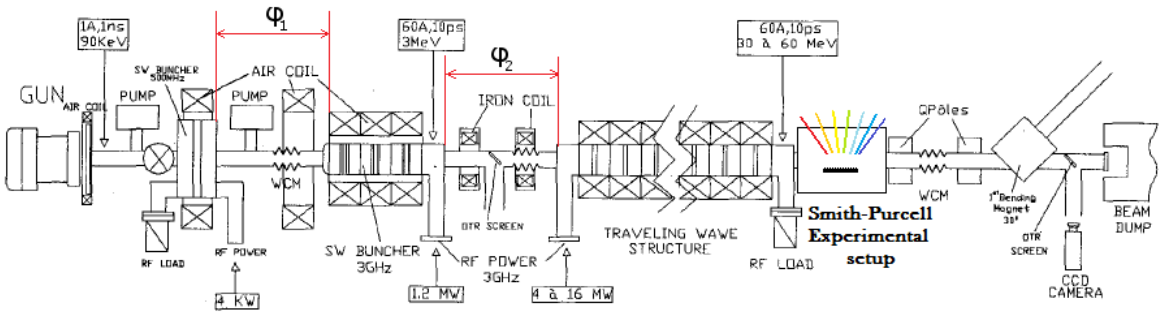


Figure 2.1: Layout of the CLIO accelerator and position of the experimental setup: $\varphi_1 = \phi_B$, $\varphi_2 = \phi_S$.

subharmonic buncher (SHB), a fundamental buncher (FB) and an accelerating cavity (AC). The gun produce bunches about 1.5 ns long at an energy of 90 keV. These bunch are then compressed by the subharmonic buncher to 200 ps or less to make it suitable for further compression with the fundamental buncher. This fundamental buncher further compresses the beam to a few ps and accelerates bunch to several MeV, making the electrons relativistic. The bunches are then further accelerated in the accelerating cavity to the operation energy (typically 10-45 MeV).

For bunch compression the most important parameters are the phases $\varphi_1$ (between SHB and FB), $\varphi_2$ (between FB and AC) and power of FB.

## 2.3 Experimental setup

The experimental setup is shown on figure 2.2. It consist of 12 pyrodetectors placed from $48^o$ to $125^o$ with $7^o$ separation. To collect the emitted radiation 25 mm diameter off-axis parabolic mirrors are used.

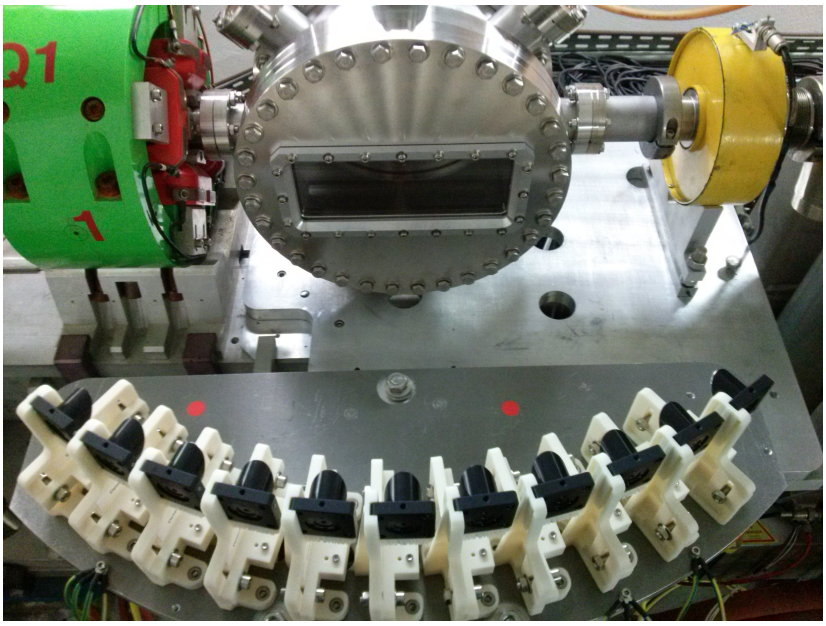


Figure 2.2: Experimental setup for SPR measurements at CLIO: set of twelve pyrodectors with off axis parabolic mirrors placed equidistantly with $7^o$ separation and experimental chamber with the grating inside.

The signal from the detectors is amplified by preamplifier, transfered to filtering/amplification board and then digitized by a data acquisition system (12 bits 1 MS/s). To connect detector preamplifier to DAQ, filter and amplify signal, we design and manufactured special device (see fig. 2.3). This device was tested and now it work successfully at CLIO. Two modification of it exist: 1MHz filter without amplification and amplification board (gain 4.5).

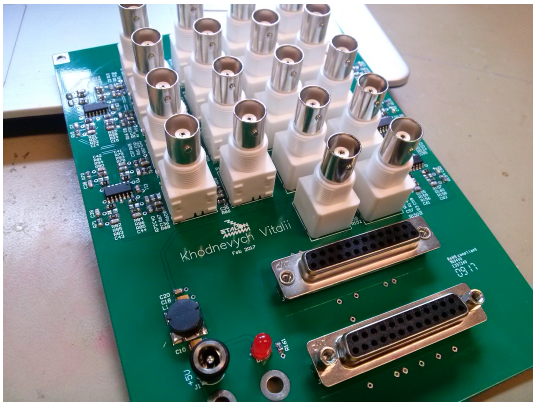


Figure 2.3: Detector-DAQ connection board (without shield).

The experiment uses a 40x20 mm aluminium grating with 3 mm and then replaced by 6 mm pitch. The beam-grating separation can be changed by a stepper motor. Position of grating is calibrated from beam center. Relative change is determined by counts of driver of stepper motor and could be measured by linear potentiometer.

A LED blinker on timer type 555 was installed to check the detection system. This allows remotely check response of pyrodetectors and DAQ.

### 2.3.1 Data Acquisition

Signal is digitazed by a DAQ board with variable sampling rate. Python script (read_plot_data.py) analyze single file with taken data and produce the the array of signals on chosen channels.

Noise filtering is implemented inside script. We use simple FFT filtering by turning in zero high frequency component of modulus of FT of the signal. Depth of filtering could be chosen by user.

Signal is extracted from filtered data on falling edge of electron signal and computed as difference of signal amplitude at equidistant positions from the edge. This give amplitude on detector when bunch pass grating and with respect to the moment before. Except this electron signal amplitude is acquired as simple min. For this type of the signal we remove constant component with FFT and leave other components as they are. After script finish his work, .sig file is generated. In this file, except spectral component and electron signal, we also have some additional information like position of the grating, time and date, etc. After measurements, .sig files are collected and analyzed by MATLAB.

Other option is online analysis with "Spectrum analyzing tool" (see fig. 2.4). It allows to monitor in online regime position of data taken, spectrum and Form factor. It has option to choose time period, position of spectrum, energy and beam-grating separation for Form factor extraction.

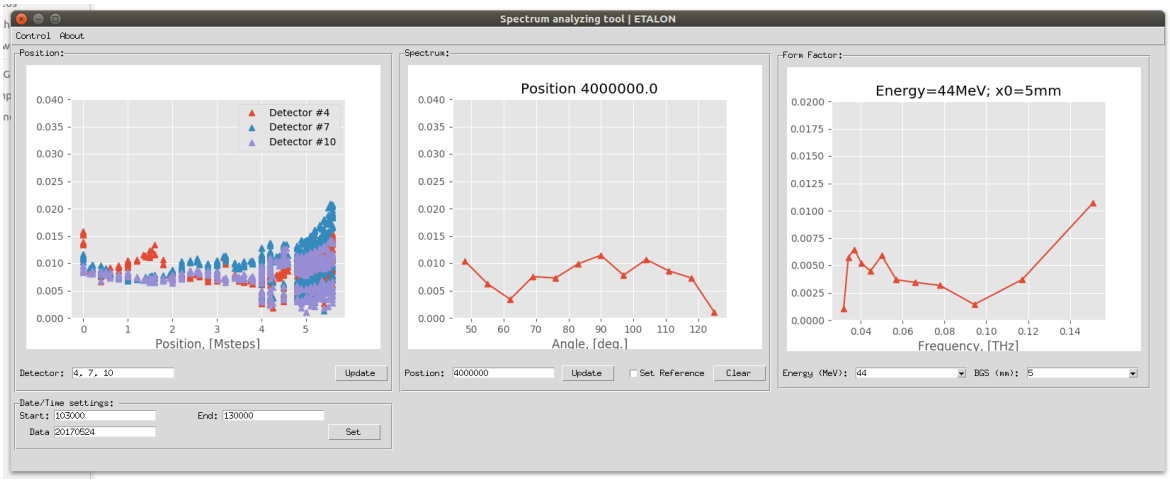


Figure 2.4: Spectrum analyzing tool. GUI was implemented on Python with Tkinter library.

## 2.4 Data processing and analysis

During measurements, in the current experimental setup, we could change only beam-grating separation (BGS). According to Smith-Purcell theory [7], we expect to see exponential decay of the signal as function of beam-grating separation (see fig.2.5). Close to the beam, signal reach saturation, as it touch the beam. Fit of this dependence will give the value of evanescent wave and will help to estimate the level of background.

We made wide scan of amplitudes for different beam-grating separation. But instead of clear exponent (linear in log scale) we see in figure 2.6 complicate curve. Result is reproducible for two different buncher phases. For different angles shape of the curve is different, but all of them have exponential increase close to beam (or linear in log scale). So, further measurements we will do in this narrow region near the beam.

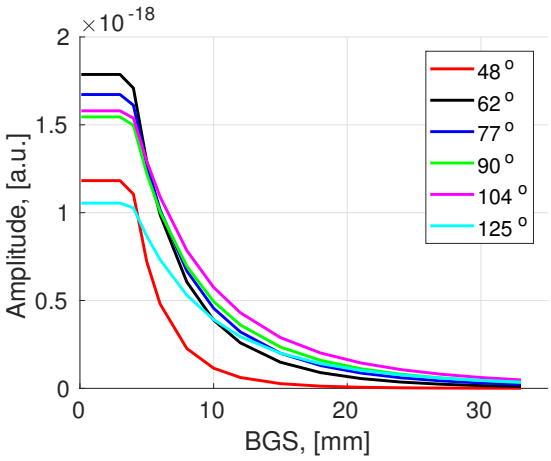


Figure 2.5: Smith-Purcell theory (gfw) prediction: Decay of SPR signal as function of BGS (gfw calculation). In calculation was used CLIO beam parameters for 3mm grating

Its clear seen from figures 2.6, that except SP signal in total signal present also background, which have non random behavior, as we could also see from figure 2.6d. Frequency at this figure was calculated for current grating (6 mm) as function of observation angle. With approaching to the beam, we saw increase of the signal (SP radiation). At region far from the beam, we see some pattern, nature of which should be investigated.

In log scale we could see in figure 2.7 two signal components: SPR signal and background. As we could see, we could measure signal only in small region near beam, which in real life could impact on beam. So background rejection technique's should be applied (THz mesh or WAP filters).

We divide signal in region of break by two subregions: background (fitted by green lines) and signal (color lines). We assume that in this narrow region background is constant, so we fit data from -Inf (approx 20 mm) to intercept of two "lines" (background and signal). This give us background level. Then we choose data points, which are higher than this level and fit them by exponent. This method allow us get better fit, when signal level is low.

In result we have three coefficients: background, amplitude of the signal and decay wavelength.

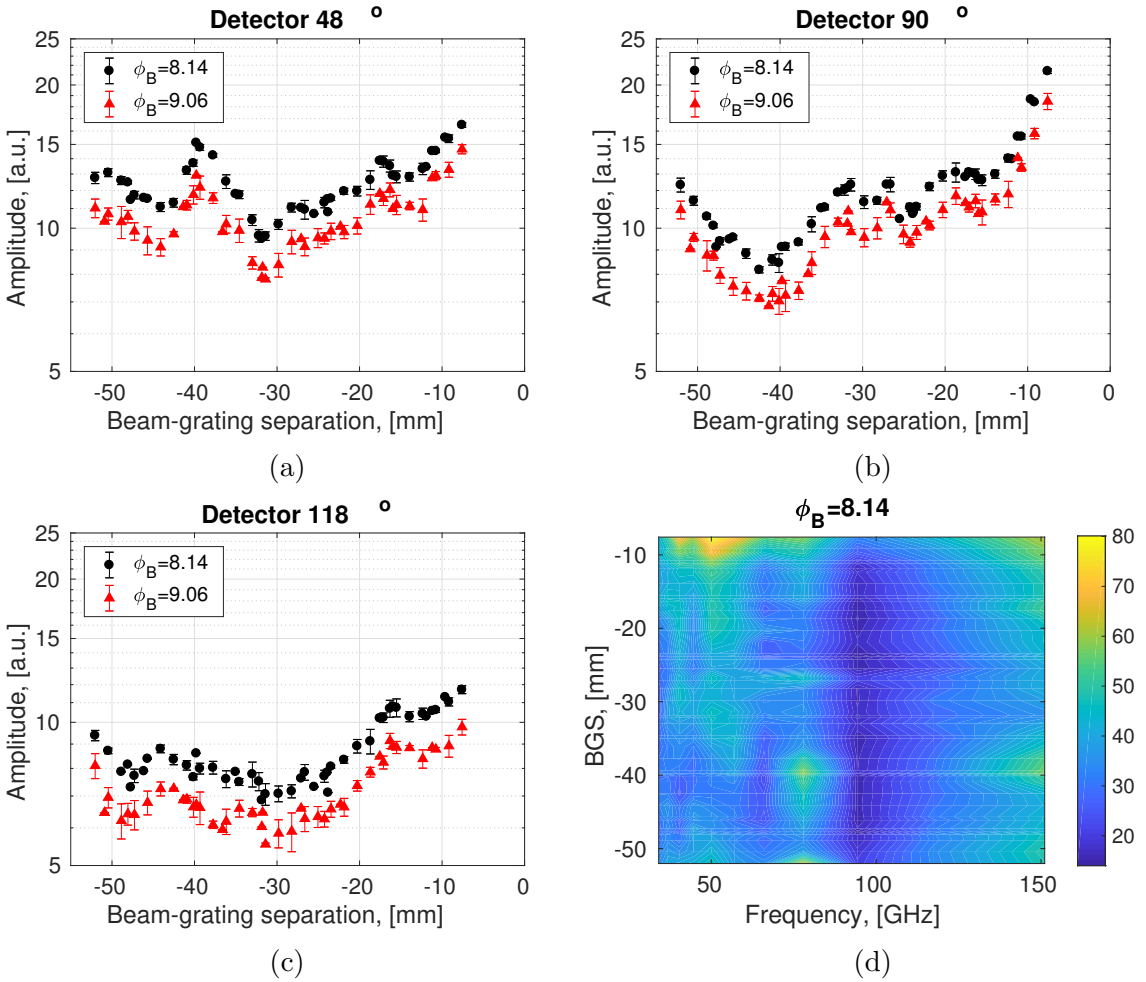


Figure 2.6: Background pattern as function of BGS for different buncher phases (wide scan, 6 mm grating, well adjusted beam). Pattern which is far from the beam is under investigation.

### 2.4.1 Buncher Phase

During first part of our experiment we change buncher phase $\phi_B$ of the accelerator. This parameter have the biggest impact on bunch length [11]. Of course this also change the intensity of electron beam. Each time signal was normalized by this value.

Value of background coefficient is also changing as function of phase. This could indicate on two thing: background is phase dependent or current analyzing method gives bad signal extraction. Of course, its not all possibilities and this phenomena should be investigated more. Reader should also take into account, that signal, which is used to fit the background was normalized by electron signal.

As was mentioned above, decay length of SP signal is angle-dependent and could be used as indicator of SPR from one side and test-check of alignment from other side. We find that in region of phase where bunch is well adjusted (see fig. 2.8a from

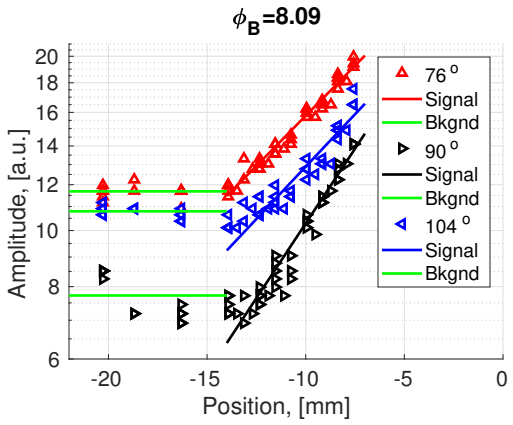


Figure 2.7: Signal and background with fits for different observation angles.

$\phi_B = 8 - 8.5$), decay wavelength is stable and phase independent, as it should be. When the signal is low, we have bad fit and distorted result. This guess could be proofed by check $R^2$ parameter of goodness of fit. Some of the measured data with bad quality of beam or specific channel have noisy data and bad fit in result. $R^2$ was used to make cut on data and correctly evaluate evanescent wavelength. From other side, Its could be also caused by change of relativistic gamma factor (energy of bunch is changing with buncher phase). From other side, this could indicate on other effect, which is measured by our system too (will be discussed later).

We take weighted mean over all the phases and compare evanescent wavelength with prediction by the theory of SPR. From figure 2.8b we see total tilt of 2 degrees.

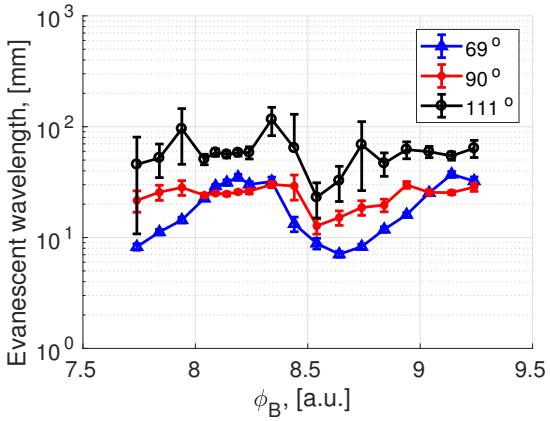


(a) Change of evanescent wavelength as function of buncher phase for certain angles

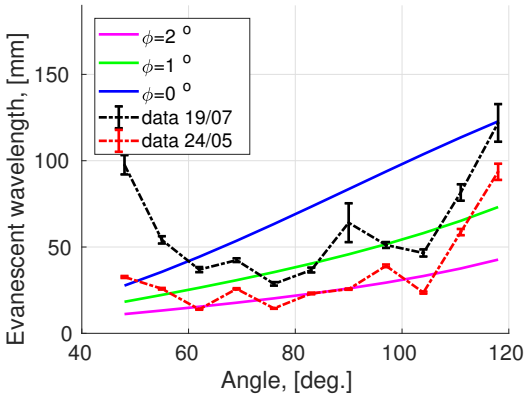


(b) Evanescent wavelength as function of angle. Black is experimental data, coulour is prediction for current grating with current $\gamma$. $\phi$ angle is azimuthal angle and Angle on X axis is polar angle $\Theta$.

Measurements at other day (19/07) confirm our assumption. At this day height of detector mount was increased by 1 cm, while individual detector alignment was kept

constant. General pattern of evanescent wave distribution was saved but moved up. So in this was, we decrease tilt by 1 degree.

Particularly it could also be caused by misalignment of the optical system. Because of long measured wavelengths, focal spot is also big, so input aperture of the OAP mirror is bigger. This correction was described in appendix and was used to extract form factor from data.

Decay length at $48^o$ is bigger than was predicted, so in this signal component could be present also some other effect. Measurements at 19/07 confirm this trend.

### Spectrum analysis

By using the fitting results, we could more precisely reconstruct the spectrum and reject the background. Using GFW code and experimental setup correction (see appendix), we could calculate single electron yield and predict spectrum for certain bunch length and shape. In figure 2.9a is shown measured spectrum for buncher phase equal $\phi_B = 8.14$ and three spectrums for gaussian beam with different bunch duration. The most suitable is 5ps gaussian bunch. Difference in width from measured one could be explained by more complex bunch structure that simple gaussian (will be discussed later). Spectrum change, as function of the phase is shown in figure 2.9b. BGS for this two spectrums is 10 mm

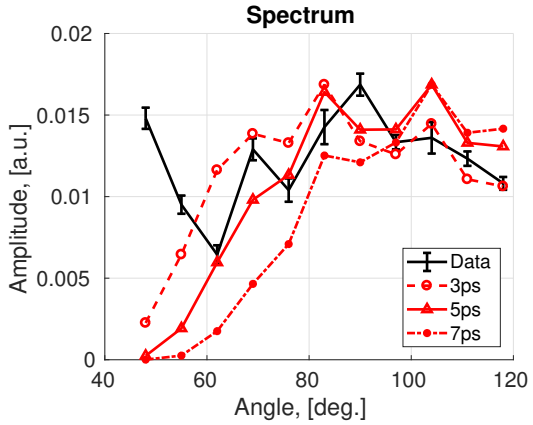


(a) Measured spectrum (black) with predicted spectrum for different bunchlengths (3, 5, 7 ps)

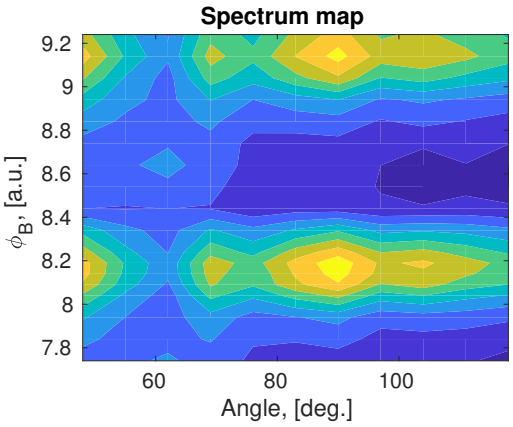


(b) Change of spectrum as function of buncher phase

Figure 2.9: Experimentally measured spectrums

### Form Factor extraction

As we know the main experimental parameters (geometry of the grating, bean energy & charge, etc), we could calculate single electron yield and then extract the Form factor. The form factor should have few features: it should not depend from beam-grating separation, which is not completely true, (see fig. 2.10b). This disagreement is not strong, as relative shape of it keep same, and amplitude could be incorrect evaluated due to different evanescent wave in computation code and experimental data.

Other feature is that it should decrease in amplitude with high frequencies. We suppose that strong components at 100-150 GHz frequency region is parasite effect, which is not belong to CSPR.

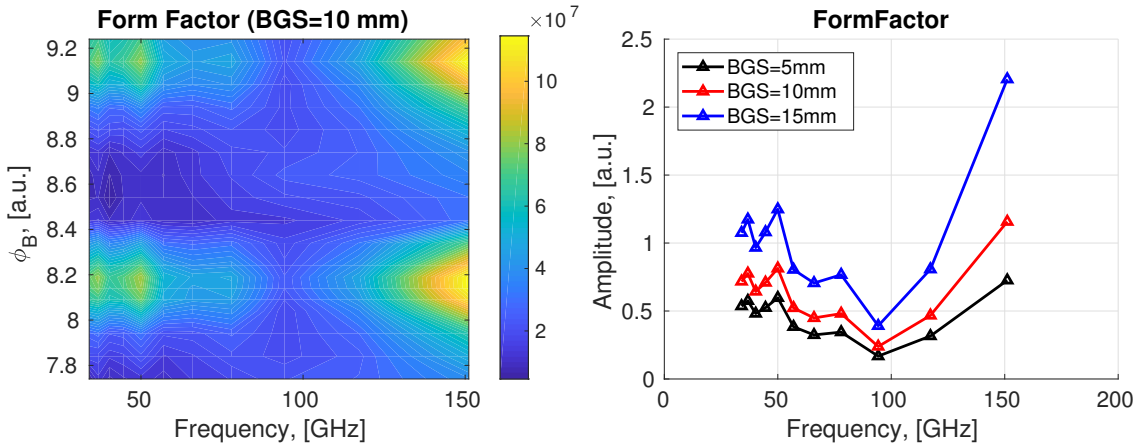


(a) Form factor map as function on buncher phase

(b) Form factor at different beam-grating separation for $\phi_B = 8.14$ buncher phase

Figure 2.10

We apply spectrum recovery procedure as was mentionned in [8]. We use most optimized bunch form-factror ($\phi_B = 8.14$) for normalization of the form-factors of others bunches. In our reconstruction we didn't take into account first two points in spectrum. The result of spectrum recovery for several bunch phases is presented on figure 2.11b.

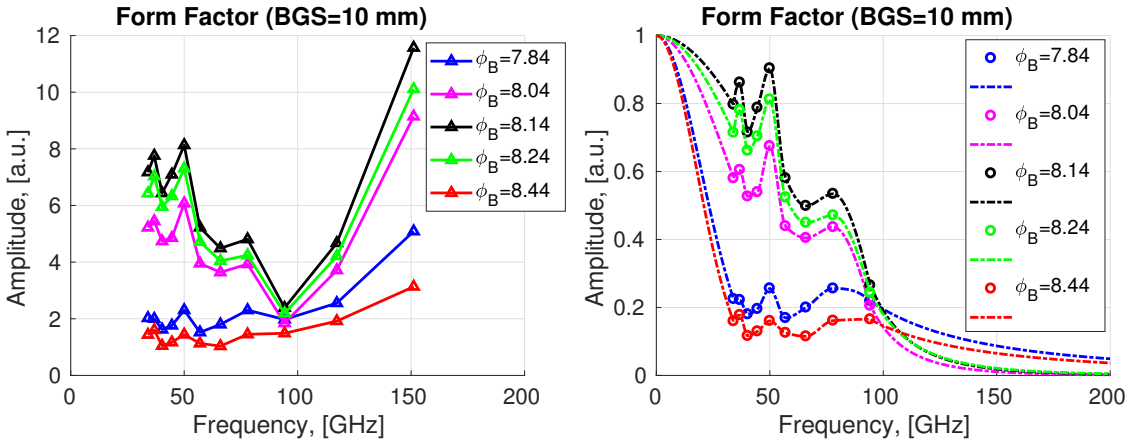


(a) Form factor at different buncher phase for certain beam-grating separation

(b) Reconstructed form factor from measured spectrum.

Figure 2.11

### Bunch profile reconstruction

Next step is profile recovery. At this point we use Hilbert method of phase recovery, as it gives the best result [8]. After we made inverse Fourier transform. Result of reconstruction is presented on figure 2.12 and 2.13b. Change of bunch width at 10%,

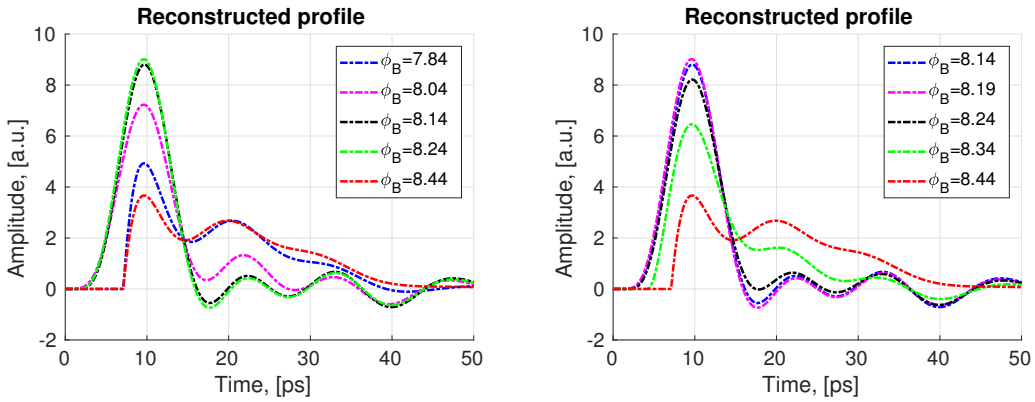


Figure 2.12: Reconstructed beam profiles for different buncher phase

50% and 90% of maximum is presented on figure 2.13a. For phase $\phi_B = 8.14$, we have: FW0.1M=2.7ps, FWHM=6.8ps, FW0.9M=11.1ps.

To check the correctness of the procedure we calculate spectrum with this reconstructed profile and compare it with measured (see figure 2.14a). The difference (blue dashed line) shows that in spectrum we have component which exponentially decrease with angle. This is background of our measurement. Nature of this component is under investigation.

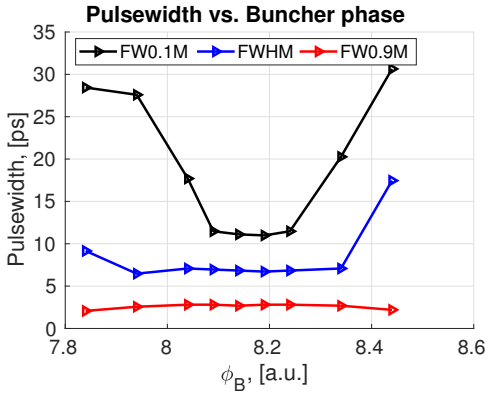


(a) Change of beam width at different level of maximum for different buncher phases

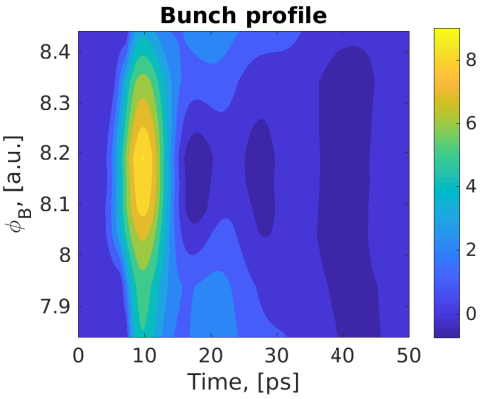


(b) Evolution of bunch profile as function of buncher phase

Figure 2.13

Also, to estimate error of profile reconstruction, we introduce noise in spectrum in calculated error bounds and reconstruct profile (set of 100 profiles, see fig. 2.14b). We get that $FWHM = 6.8 \pm 0.3ps$ within 3 sigma change of the spectrum components.

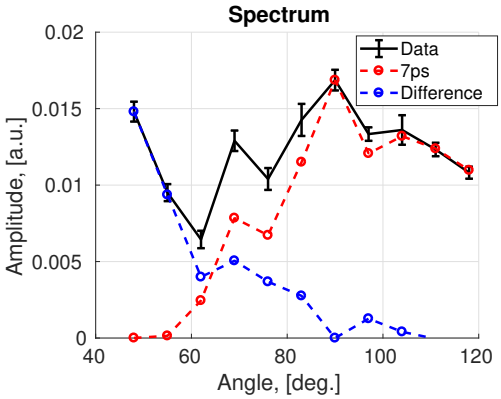


(a) Comparison of measured spectrum (black), calculated from reconstructed profile (red) and difference (blue)

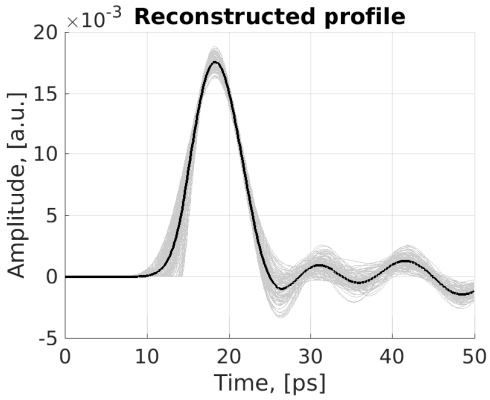


(b) Mean (black) of reconstructed profiles (gray) with introduced noise in form factor

Figure 2.14

Results are agreed with previous measurements [12].

### 2.4.2 Buncher power

Same study was done for spectrum's as function of buncher power. We made same procedure of data extraction, but get other behaviour of coefficient. Coefficient stay constant until reaching the bunch power equal 1.2 (see figure 2.15a).

As "theoretical" we suppose increase in bunch energy from 38.2 MeV for 1.2 [a.u.] of buncher power to 44.2 MeV at maximum buncher power. In this range of energies, evanescent wavelength almost not change (small decrease), as shown on figure 2.15a by solid line. In general, evanescent wavelengths are in the previous trend (see fig. 2.15b)

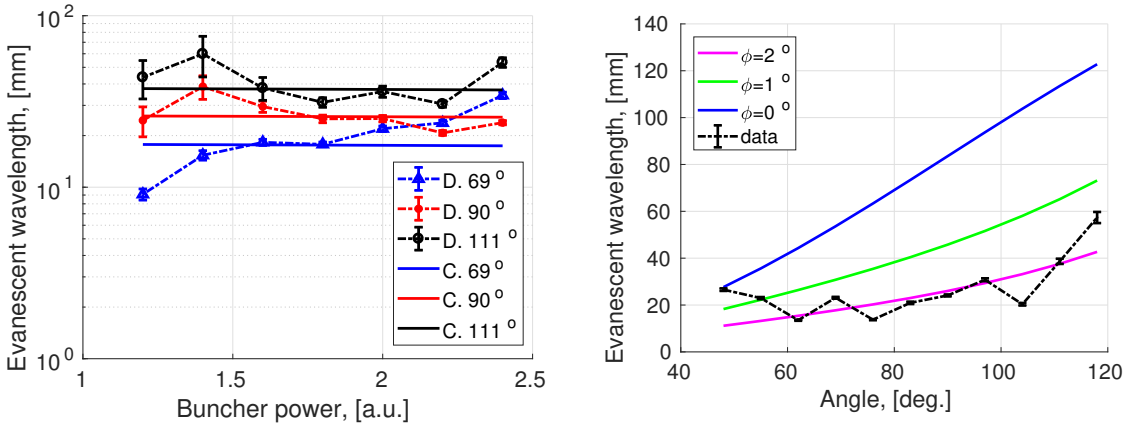


(a) Change of evanescence wavelength as function of buncher power

(b) Weighted mean evanescence wavelengths as function of observation angle

Figure 2.15

Spectrum change as function of buncher power is presented in figure 2.16. With low power of buncher, It is impossible to form "good bunch" for further acceleration.

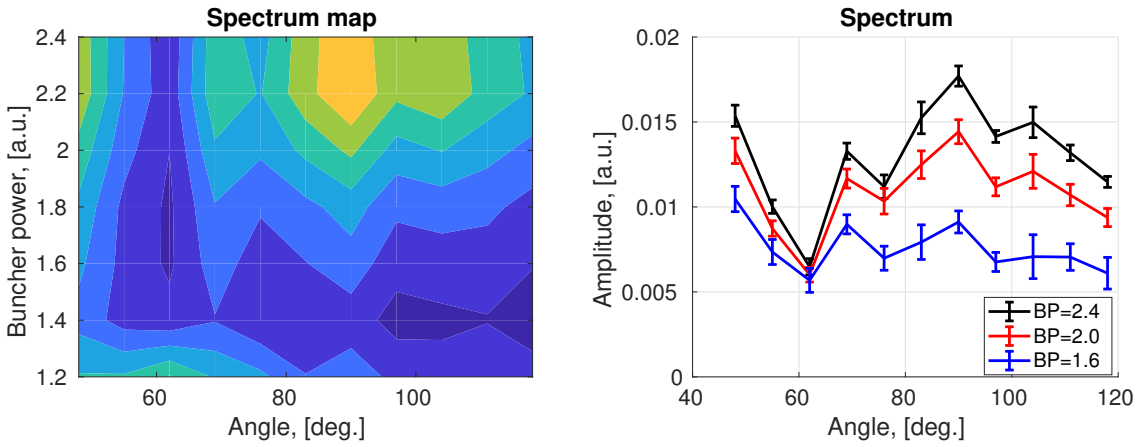


(a) Change of spectrum with buncher power

(b) Spectrums for different buncher power

Figure 2.16: Spectrum change as function of buncher power

FWHM and FW0.1M ( see fig. 2.17a)not really depend from buncher power, but FW0.9M increase almost twice with decrease of buncher power. That indicate on bad compression of tail of the bunch.

Profile evolution is presented on figure 2.17

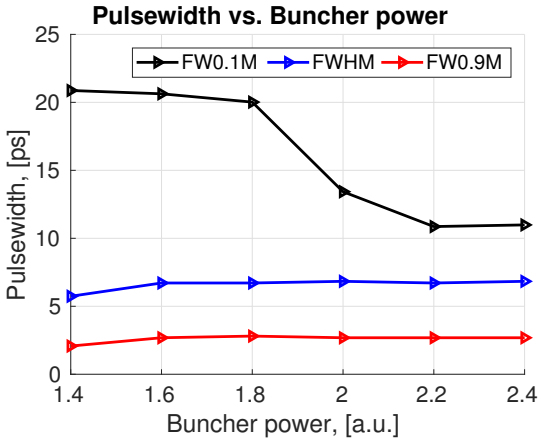


(a) Evolution of bunch width with buncher power

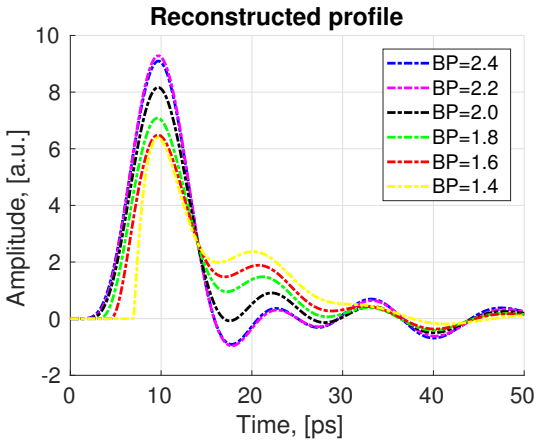


(b) Reconstructed profiles

Figure 2.17: Evolution of bunch profile with buncher power

### 2.4.3 Section phase

Variation of the section phase have small impact on bunch shape (see fig. 2.19b), but its increase significantly energy of the bunch. Section phase on plots is in units of hundreds from value which we get in control room of accelerator. Spectrum map is in figure 2.18.

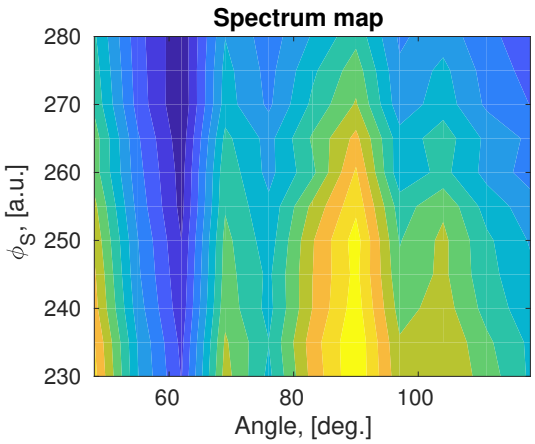


Figure 2.18: Change of spectrum with section phase

Scan of the section phase was done not over $2\pi$, but even in this region, we see impact of phase on tail width of the bunch (see fig. 2.19a).

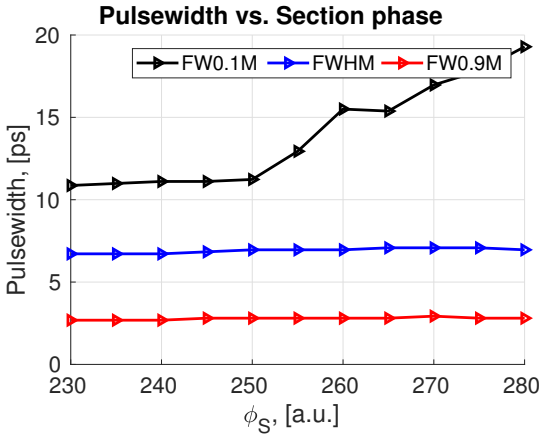


(a) Evolution of bunch width with section phase

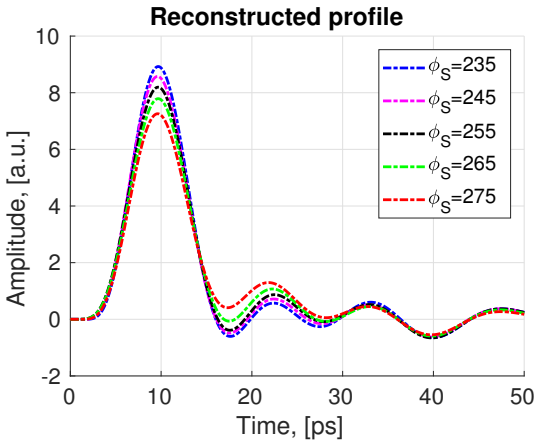


(b) Reconstructed profiles

Figure 2.19: Evolution of bunch profile with section phase

# Chapter 3

# THz filters

Precise measurements of the beam profile with Smith-Purcell radiation require precise measurements of the spectrum. To filter background signal from Smith-Purcell radiation we will use inductive mesh filters. Detector unit at each angle will have its own filter, which correspond to the emitted wavelength of Smith-Purcell radiation.

## 3.1 Mesh filters

Metal-mesh filters are filters made from the metal meshes (see fig. 3.1a). They work in diapason from far infrared to submilimeter regions of the electro-magnetic spectrum. We use inductive mesh filters. This means that they are band-pass filters. Transmissivity function is presented in figure 3.2. Using Ulrich's [13] theory we calculate mesh parameters (period, thickness of wire(strip); see fig. 3.1a) for certain frequencies. Example of manufactured filters is present in figure 3.1b.

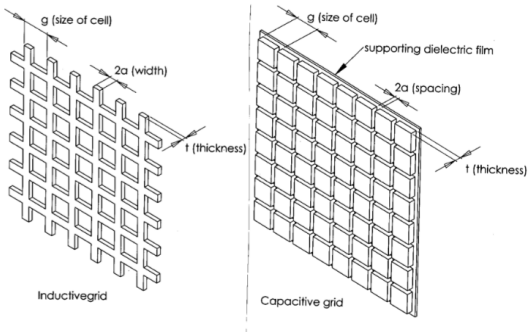


(a) Inductive and capacitive mesh filters (image source: wikipedia)

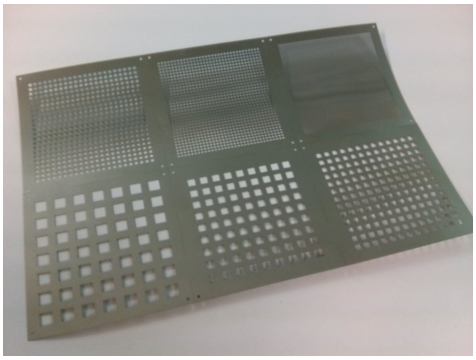

(b) Manufactured THz filters

Figure 3.1: Mesh filters

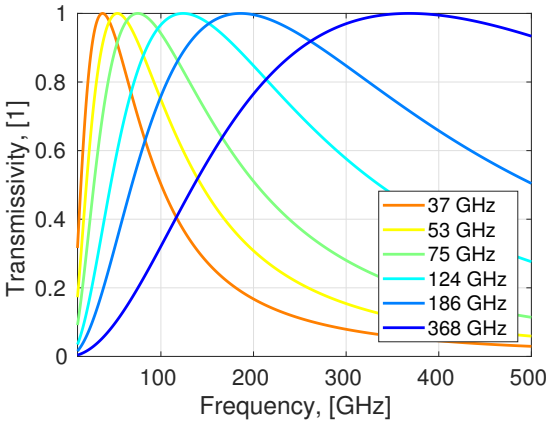


Figure 3.2: Transmissivity functions of inductive mesh filters

### 3.1.1 Experimental check of filter properties

To test the filters we use setup, as present on figure 3.3. We test filters with two GHz sources: GDO-2510F on 24GHz and SOL-3510-28-G1 on 35 GHz. Setup consist of source (S), chopper with frequency 25 Hz (result is independent from chopper speed), filter frame (F) with or without filter, and detector (D) with connected Horn anthena (A). Measurements can be done also without chopper.

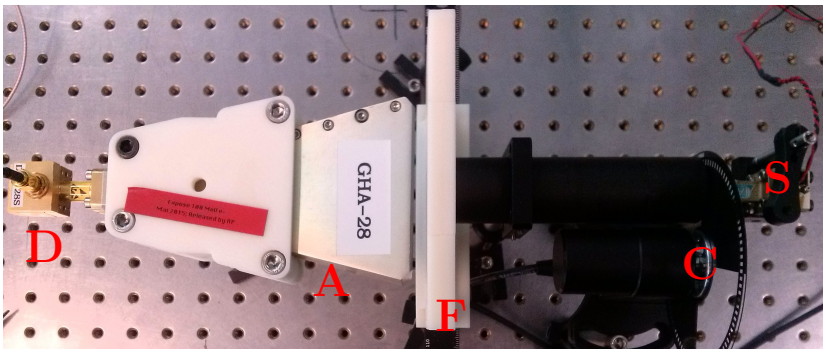


Figure 3.3: Experimental setup: S - GHz source, C - chopper (25 Hz), F - frame for filter, A - Gain Horm Anthena (GHA-28), D - detector (DET-28S)

To acquire the signal we use RTM 2054 Oscilloscope. We measure peak-to-peak voltage (Vpp) on detector. The order of the measurements was following: measure Vpp without filter; install filter and measure Vpp with filter. Ratio with and without of Vpp gives Trasmissivity for current filter. Due to big wavelength position of parts of the experimental setup play a big role.

Due to unknown spectral characteristics of detector and both sources, we could not compare experimental results with our calculation, but can assume gaussian spectrum of the source and flat frequency sensitivity of detector. Results are present on figures 3.4. We have good agreement of calculation and experiment (see fig. 3.4). With small

correction of filter impedance, agreement is even better for both sources.

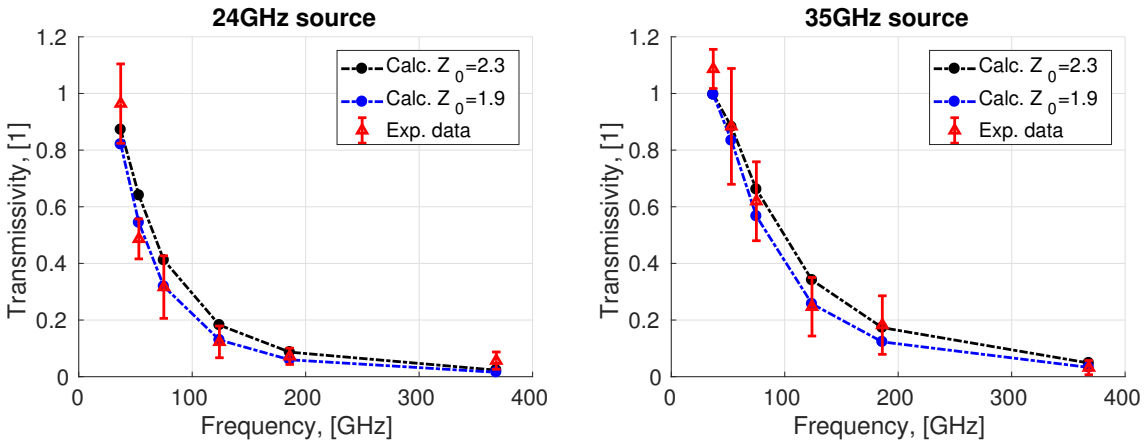


(a) (b)

Figure 3.4: Experimental results: Transmissivity

## 3.2 Cross-Mesh Filters

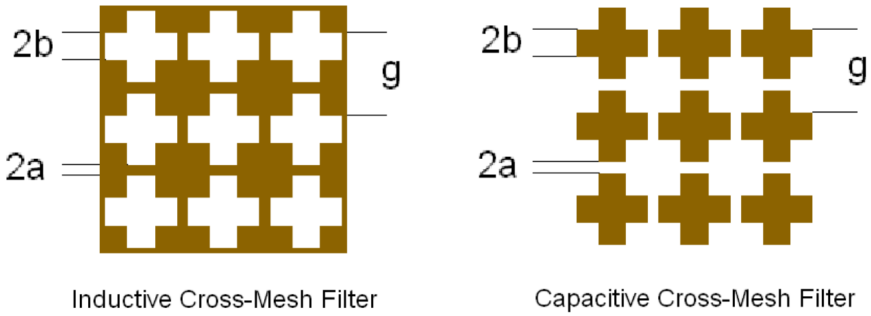


Figure 3.5: Cross-mesh filters layout (from [14])

Cross filters layout is presented in figure 3.5. Characteristic sizes (g,a,b) determine filtering frequency and width of transmissivity function. On resonant wavelength

$$\lambda_r = 2.27g - 4a - 2b$$

transmission is zero for capacitive filter and one for inductive cross-mesh filter.

We will be interested only by inductive filters. Characteristic impedance in this case is:

$$Y(f) = \frac{1}{a_1 \pm i\frac{gA_1}{\lambda_r \Omega(f)}}$$

where $a_1 = 0.0001$ is metal loss parameter and $A_1 = 0.53$ is bandwidth parameter. Normalized frequency is

$$\Omega(f) = \frac{\lambda_r f}{c} - \frac{c}{\lambda_r f}$$

### 3.2.1 Matrix methods

To determine the transmittance and reflectance of cross filters matrix method is used. Systems with several filters will be reduced simple matrix multiplication. Filter scattering matrix depends only on the impedance of equivalent circuit (see fig. 3.6).

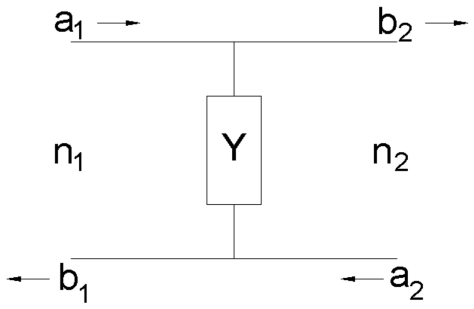


Figure 3.6: Equivalent circuit of cross filter (image source: [14])

Incident wave $a_1$ and reflected wave $b_1$ on the l.h.s. relate to the wave amplitudes $a_2,\ b_2$ on r.h.s. by following matrix:

$$\begin{pmatrix} b_1 \\ a_1 \end{pmatrix} = \begin{pmatrix} S_{11} & S_{12} \\ S_{21} & S_{22} \end{pmatrix} \begin{pmatrix} b_2 \\ a_2 \end{pmatrix} \tag{3.1}$$

If $a_2 = 0$, transmission coefficient

$$t = \frac{b_2}{a_1} = \frac{1}{S_{22}}$$

. By applying Kirchoff's laws we could find $S_{ij}$ elements:

$$S = \begin{pmatrix} -\frac{Y(f)}{2} + 1 & -\frac{Y(f)}{2} \\ \frac{Y(f)}{2} & \frac{Y(f)}{2} + 1 \end{pmatrix} \tag{3.2}$$

As Y is frequency-dependent, so transmittance also will be frequency dependent.

In case of series of elements, we multiply scattering matrix of each element $S_{total} = ...S_3S_2S_1$. Transport matrix (in medium between filters):

$$T = \begin{pmatrix} e^{-\frac{2\pi i f d}{c}} & 0 \\ 0 & e^{\frac{2\pi i f d}{c}} \end{pmatrix} \tag{3.3}$$

where d is distance between filters. In case of repetitive system of several filters $S_{total} = ...S_3T_{32}S_2T_{21}S_1$. Transmission coefficient in this case calculated from $S_{total}$ matrix.

In calculation code also taken into account change of refractive index from medium to medium (in case filter is grown on substrate), angle of incident wave fall, loss of propagation between filters, polarization angle of incident wave.

Change of transmissivity as function of geometrical parameters a and b are presented on figures 3.7a and 3.7b.

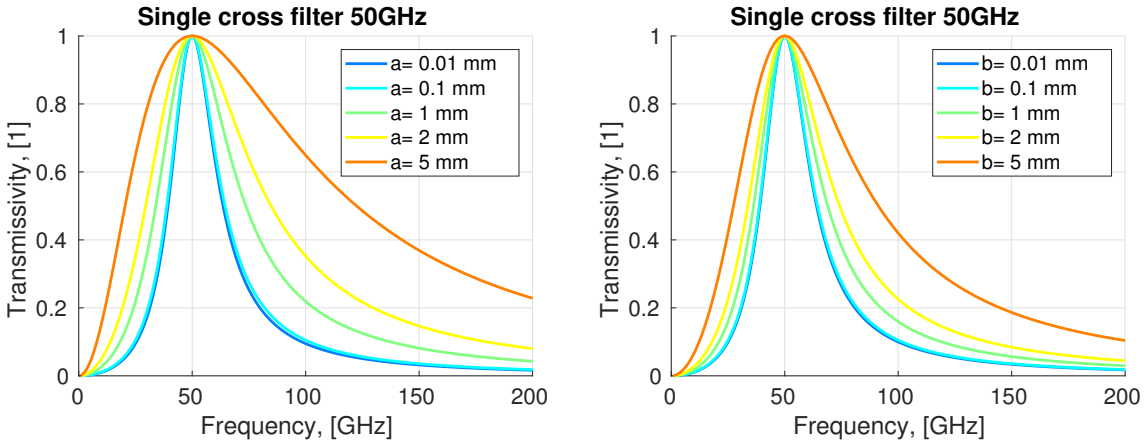


(a) Change of transmissivity as function of geometrical parameter a

(b) Change of transmissivity as function of geometrical parameter b

Figure 3.7

### 3.2.2 Experimental check of filter properties

For experimental check of cross-mesh filter properties, was used same RF sources: on 24 and 35 GHz. For this purpose we designed designed 16 filters(see fig. 3.8). The

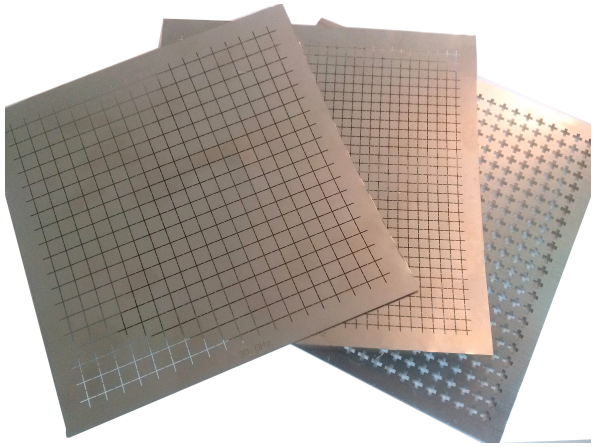

Figure 3.8: Manufactured test cross-mesh filters: left filter is 30 GHz, middle is 50 GHz, a=0.1 and right is 50 GHz, a=0.5

experiment consisted in two parts:

- Test transmissivity of filters as function of filter frequency (see 3.9a and 3.9b )
- Test transmissivity of filters as function of a,b parameters for fixed filter frequency (see 3.10a and 3.10b )

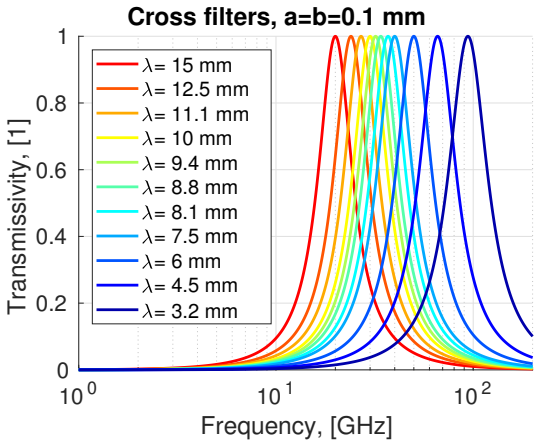


(a) Transmissivity functions for different test wavelengths

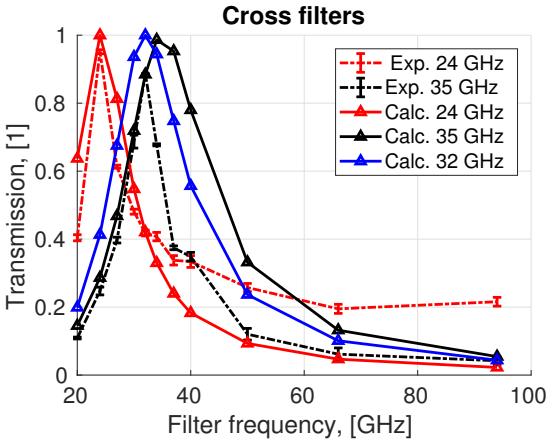


(b) Transmission for different filter with present sources: dashed is experimental data, solid is calculation.

Figure 3.9: First part of the experiment: checking of transmission

Agreement between calculation and measurement is achieved.

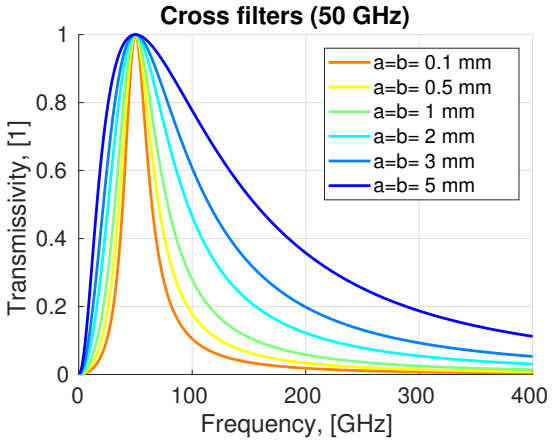


(a) Transmissivity functions for different filter parameters

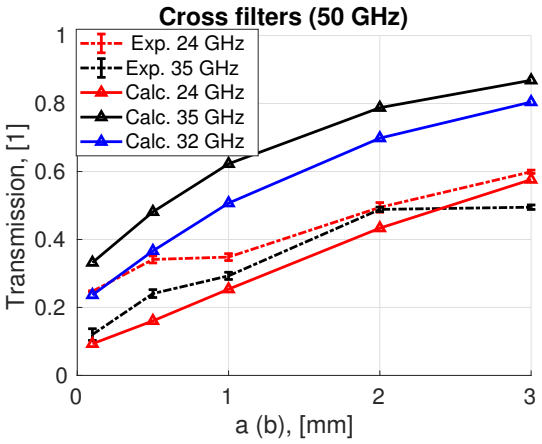


(b) Transmission for different filter with present sources: dashed is experimental data, solid is calculation.

Figure 3.10: Second part of the experiment: checking of filters parameters dependence

### 3.2.3 Multiple filters

To decrease tails of transmissivity functions, possible to use several cross filters. On figure 3.11a is shown transmissivity for single, double and triple filters. Double filters significantly decrease tails but produce narrow window in the region far from resonant frequency. Triple filters didn't give big effect, but require more filters in realization. So we will use double cross filters.

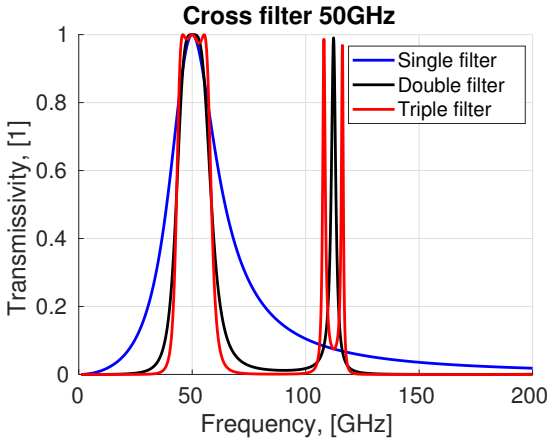


(a) Transmissivity function of single, double and triple cross filters

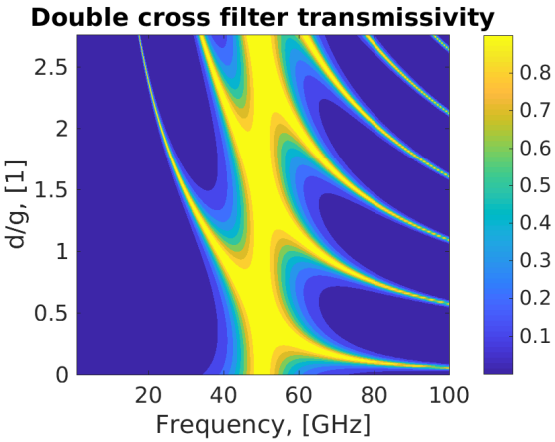


(b) Change of transmissivity function for double cross filters as function of filters separation

Figure 3.11: Multiple filters

Question which arise is at which optimal distance put second filter with respect to the first one. We find (see 3.11b) that when filters separation is equal to the half of g

parameter, transmissivity function have the best characteristics.

### 3.2.4 CLIO filters

Using matrix method for calculation of the cross filters we could calculate single and double structure filters for Smith-Purcell experiment at CLIO. Filter size is 3x3 $cm^2$. Filter separation is equal to the half of g parameter. Frequency of the filters are calculated for current setup ($7^o$ detector separation, 6 mm grating). Transmissivity functions are presented on figure 3.12.

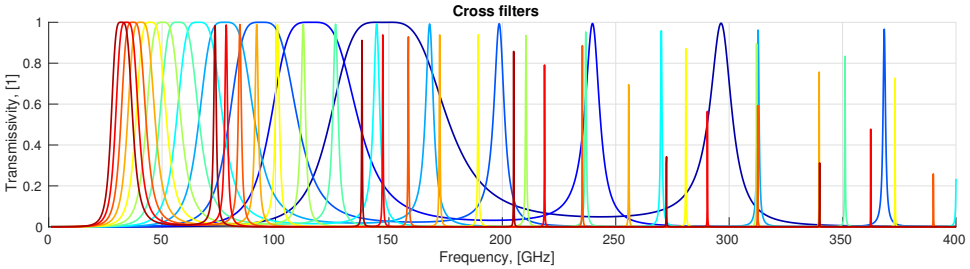


Figure 3.12: Transmissivity functions of cross filters for Smith-Purcell experiment at CLIO.

Usage of filters give big advantages for experiment, as it significantly cut background components of the signal. But it's also require more precise alignment. Shift of the detector mount with respect to the grating base cause decrease of signal (as detector then aligned on other frequency and filters stay at designed). As wavelengths of Smith-Purcell radiation are distributed by cosine law, shift of setup in one or other side is not same (see fig. 3.13). To estimate this effect we calculate the ratio of transmitted fraction of radiation with and without the filters. Integration borders are determined by the acceptance of detection system (25mm OAP + pyrodetector). Result of this calculation are presented on figure 3.13. We conclude that even with error of detector system mount, we still should detect more than 90% of emitted radiation.

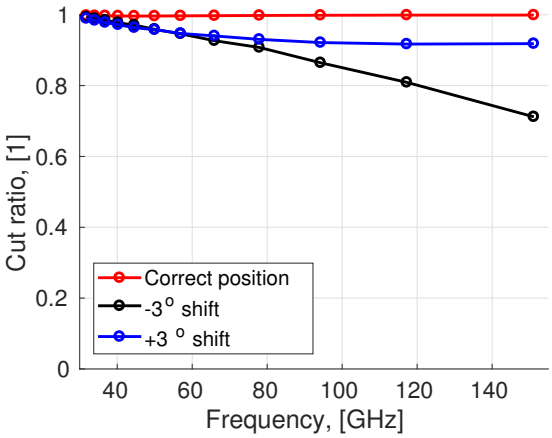


Figure 3.13: Impact of detectors shift on fraction of measured radiation with double cross filters

# Chapter 4

# SPESO

The Smith-Purcell Experiment at SOLEIL (SPESO) allows parasitically measure Smith-Purcell radiation in the SOLEIL Linac.The experimental setup is shown on figure 4.1. Is was upgraded in 2016 with one of the radiation detector replaced with a Gaussian Optics Antenna for measurements of both polarization components. This antenna has a $3.5^o$ angular resolution. It is mounted on three translation stages and two rotation stages allowing to move it around the interaction point along 5 degrees of freedom. To detect the CSPR signal we also use Gunn diode detector (MOT-22S) with Horn antena (Det3 in figure 4.1).

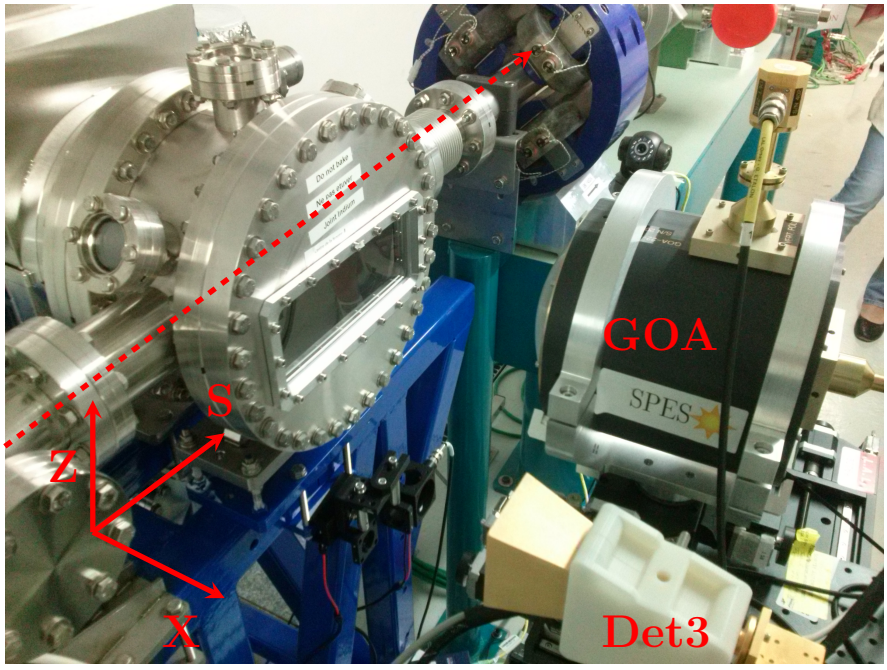


Figure 4.1: The SPESO experiment in the SOLEIL Linac. Red dashed line shows electron beam propagation direction. Gunn detector (Det3) and GOA are installed on 3D translation stage, both on individual 2D rotation stage. In front of them is installed experimental chamber within 10 mm pitch grating.

## 4.1 Polarization measurements

To estimate the polarization, we calculate degree of polarization as:

$$D = \frac{S_V - S_H}{S_V + S_H}$$

where $S_V$ and $S_H$ are vertical and horizontal components of the signal.

Theory of Smith-Purcell radiation [7] predict domination of vertical component of polarization with gap in degree of polarization around $40^o$ (see figure 4.2). We would like to check this property in our experiment.

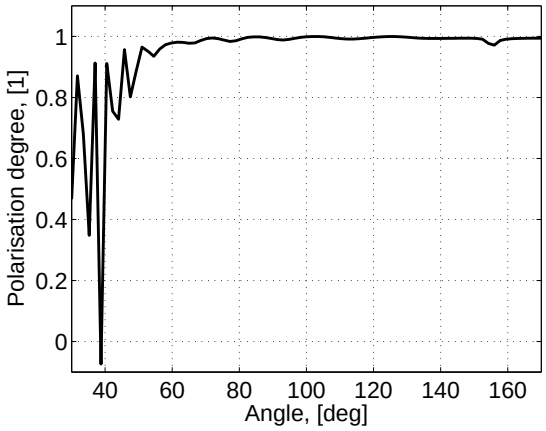


Figure 4.2: Degree of polarization as function of angle for a 20x90 mm grating with 10 mm pitch, and a 10 mm beam-grating separation and for relativistic $\gamma = 200$

Pulses only in short pulse mode mode are visible with polarizer (due to weak signal and low sensitivity of detectors). Experimental results for both polarizations are presented in figure 4.3.

During measurements of this spectrums, we change position of the detector and rotate it in horizontal plane (RS3). When detector is not rotated, it see only one frequency and small change of the borders of the grating (discussed in appendix). With $3.5^o$ angular acceptance of polarizer (efficiently small) we have exactly this situation.

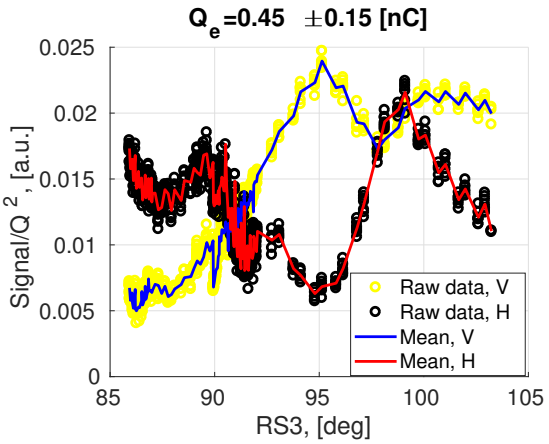


Figure 4.3: Measured SPR spectrum from the end of April to June 2017 date as function of angle calculated from detector rotation RS3.

For the same cuts as for signal, we check background polarization (when grating is retracted, see fig. 4.4a). We could conclude that background in non polarized. Results of degree of polarization for this data are presented in figure 4.4b.

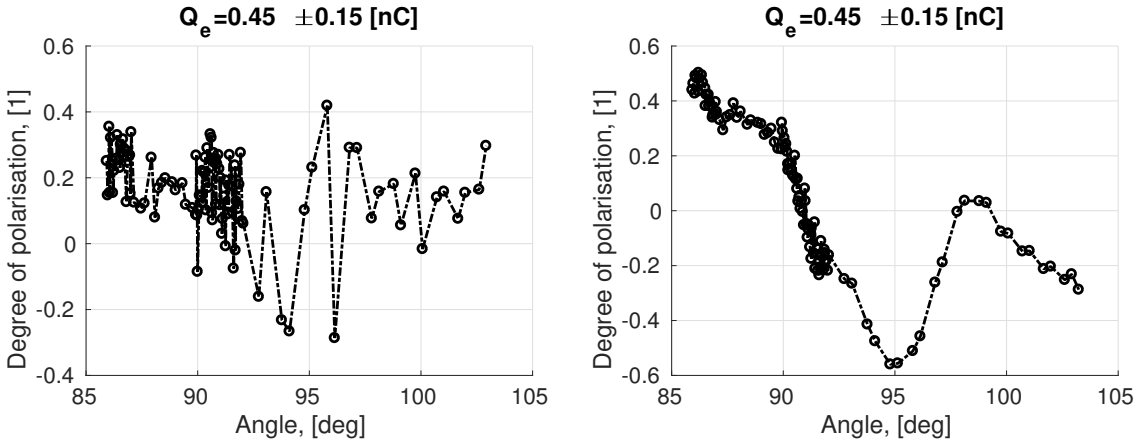


(a) Polarization of SPR background (b) Polarization of SPR

Figure 4.4: Experimental results. Degree of polarization

This results don't agree with our model (see fig. 4.2), so advanced model of SPR should be developed.

### 4.1.1 Polarization measurements with shift in Z axis

In this part of the experiment we measure spectrums in different vertical position, which is almost equivalent to measurements at different azimuthal $\phi$ angles ([7]). Same corrections as for S axis (direction of the axis see in figure 4.1), could be applied to Z axis (see Appendix). As grating is not wide, boundary effects are strong and we could observe change of the spectrum with change ofthe detector height. Increase of the height cause decrease of signal amplitude and change of spectral components (see fig. 4.5), while the polarization is almost constant (see fig. 4.5f). Measurements are not symmetrical to azimuthal displacement. Working height is Z=1.45 ($\phi \approx 0$).

Interesting to note that polarization is slightly changing with vertical displacement.

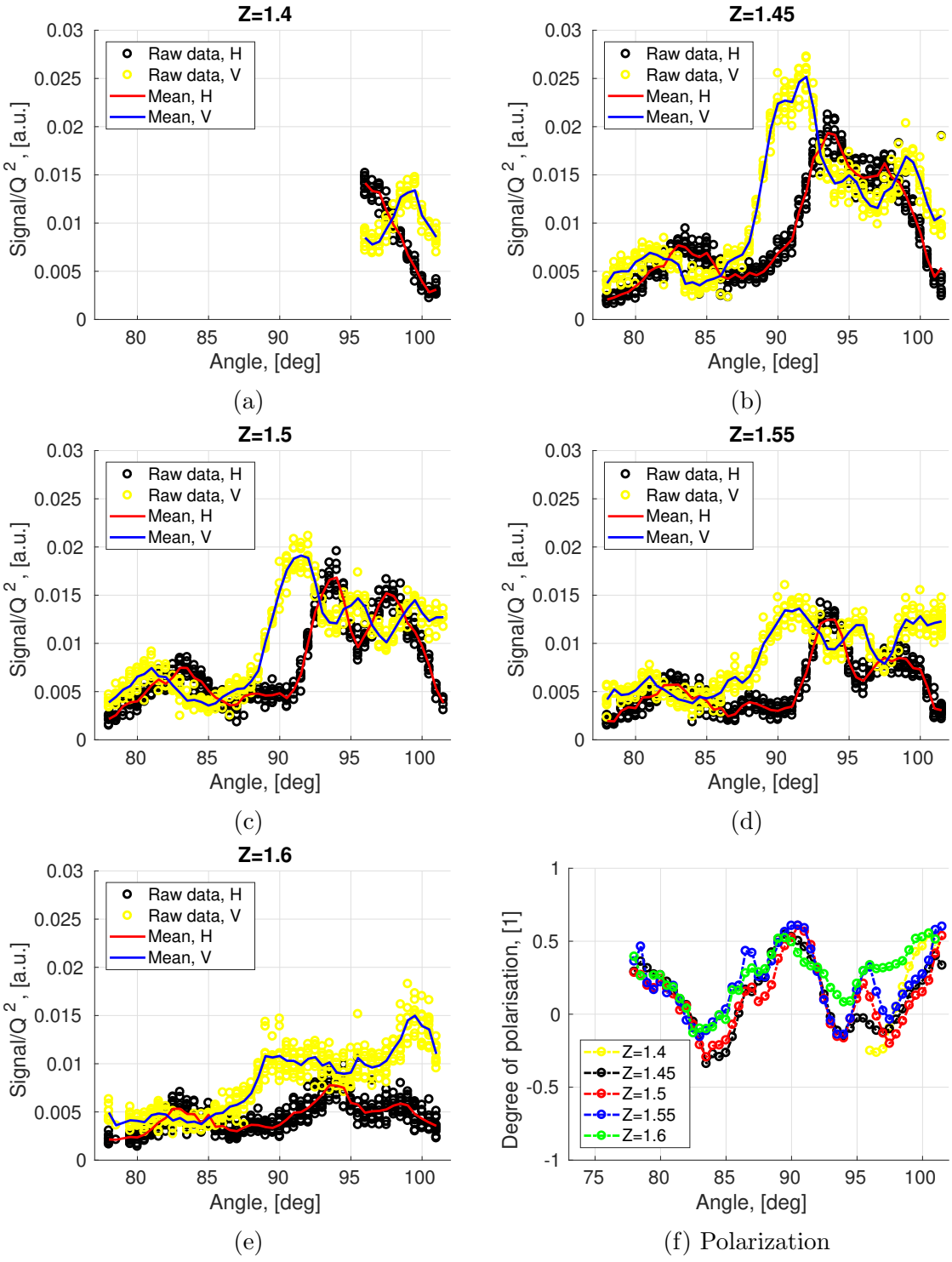


Figure 4.5: Experimental results. SPR spectrums as function of vertical detector displacement.

# Chapter 5

# Conclusion

We have observed at the CLIO Free Electron Laser a signal that is compatible with Coherent Smith-Purcell Radiation and that depends on the buncher and section phase, buncher power. Our current setup does not allow a full reconstruction of the bunch profile but an upgrade is underway.

Double cross-mesh filters will be installed. Experimental check of mesh and cross-mesh filters properties gives good agreement between calculation and measurements.

Also at SOLEIL we have made a first measurement of the polarization of Smith-Purcell radiation. The results are promising but require further investigations that are on-going.

Results of work was presented at IPAC17.

# Bibliography


[1] Vitalii Khodnevych, Nicolas Delerue et al. *Study of a Smith-Purcell Radiation-based longitudinal profile monitor at the CLIO Free Electron Laser.* IPAC17, MOPAB026

[2] Nicolas Delerue, Stéphane Jenzer, Vitalii Khodnevych et al. *Measurement of the polarisation of Coherent Smith-Purcell Radiation in the SOLEIL Linac* IPAC17, MOPAB025

[3] Nicholas Matlis, M. Bakeman, C. G. R. Geddes, T. Gonsalves, C. Lin, Kei Nakamura *Ultrafast Diagnostics for Electron Beams from Laser Plasma Accelerators*,AIP Conference Proceedings 11/2010

[4] Nicolas Delerue, George Doucas, Ewen Maclean and Armin Reichold *Longitudinal bunch profile diagnostics in the 50fs range using coherent Smith-Purcell radiation.* ,Accelerator Physics (physics.acc-ph); Instrumentation and Detectors (physics.ins-det), JAI-2009-004

[5] S. J. Smith and E. M. Purcell, Phys. Rev. 92, 1069. Published 1953.

[6] P. Rullhusen, X. Artru, P. Dhez *RADIATION SOURCES USING RELATIVISTIC ELECTRONS* World Scientific Publishing Co. Pte. Ltd, Singapore, 1998.

[7] J. H. Brownell, J. Walsh, and G. Doucas. *Spontaneous Smith-Purcell radiation described through induced surface currents.* In: Phys. Rev. E 57 (1 Jan. 1998), pp. 1075–1080. doi: 10.

[8] N. Delerue , V. Khodnevych et al. *Study of phase reconstruction techniques applied to Smith-Purcell radiation measurements.* IPAC2014, THPME088

[9] J. C. Bourdon et al. *CLIO: FREE ELECTRON LASER IN ORSAY.* In: Particle accelerator. Proceedings, 1st EPAC Conference, Rome, Italy, June 7-11, 1988. Vol. 1, 2. 1988.

[10] Vitalii Khodnevych, Nicolas Delerue et al *Comparison of Coherent Smith-Purcell Radiation and Coherent Transition Radiation* IPAC16, MOPMB003

[11] Nicolas Delerue,Stéphane Jenzer, Vitalii Khodnevych et al. *Study of short bunches at the Free Electron Laser CLIO* IPAC16,MOPMB005

[12] F.Glotin, J.-M.Berset,R.Chaput, D.A.Jaroszynski, J.-M.Ortéga, R.Prazérès *Bunch length measurements on CLIO* Nuclear Instruments and Methods in Physics Research Section A: Accelerators, Spectrometers, Detectors and Associated Equipment, Volume 341, Issues 1-3, 1 March 1994, Pages 49-53

[13] R. Ulrich, *Far-infrared properties of metallic mesh and its complement- ary structure*, Infrared Physics, Vol. 7, pp. 37-55, Pergamon Press Ltd. 1967, Printed in Great Britain.

[14] Benjamin Hooberman *Everything You Ever Wanted to Know About Frequency-Selective Surface Filters but Were Afraid to Ask*, May 2005

# Appendix

## Corrections for SPESO

Current experimental setup require careful geometrical correction. First step, is taking into account limit size of grating (see fig. 1). We divide the problem in two parts: when both sides of detector see the grating (green lines) and when only one half of detector saw it (red lines). So in case detector move parallel to the grating, angles of grating borders are changing respectively to observation point. United for both cases result present on figure 2. Here $\alpha_1$ and $\alpha_2$ are angles from which detector saw grating borders when it move along S axis (real SPESO dimention was taken into account).

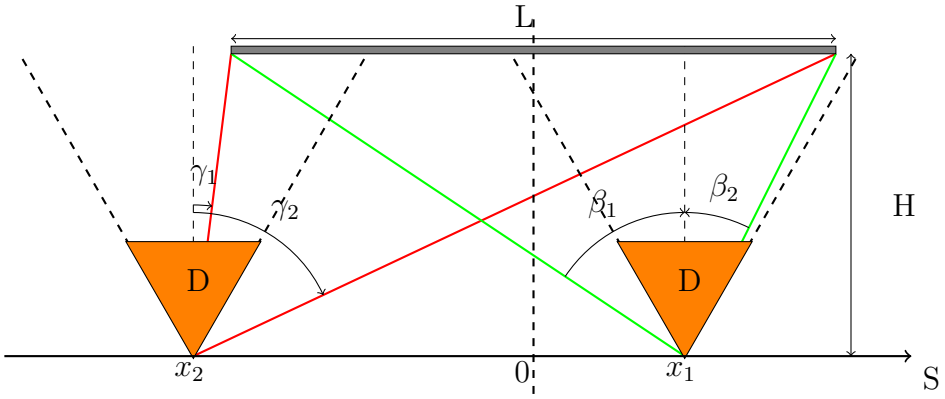


Figure 1: Geometrical corrections

Second step is to take into account angular acceptance of detector when its not rotating (green, dashed lines on fig. 2). Rotation of detector change angular acceptance and integrated region of frequencies in signal integral. Reared should note, that without rotation and with small angular acceptance, this frequency region will be the same along all grating, up to grating borders. From other side, current model is for infinite grating and exact impact of finite grating size should be investigated.

Third step is taking into account grating rotation, which is simple shift in angular acceptance.

Using all this correction, we are able to calculate correctly signal of SPR from current (gfw) model

## Correction on defocusing

If grating is in focus of OAP mirrors, all detectors see centers of the grating (see fig. 3a). Turned by defined angle, mirror saw bigger grating surface (represented by red ellipse on the schema). If grating is small, ellipse could be bigger than grating. Cross-section of ellipse and rectangular define this correction.

Except this, grating could move along X direction (closer and far from the beam). Depending where grating is, its also define correction on defocussing.

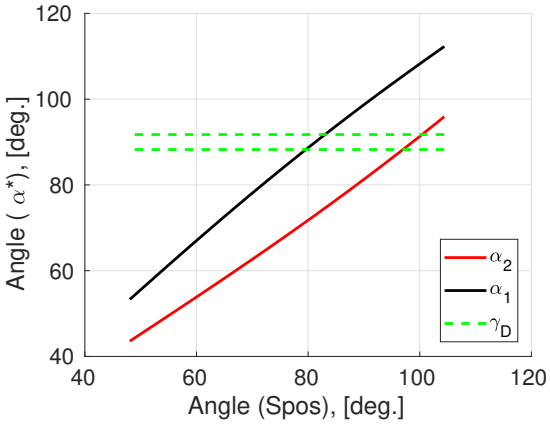


Figure 2: Geometrical corrections

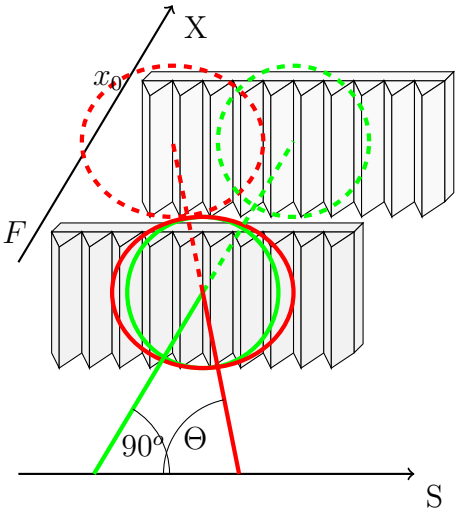


(a) Correction of defocusing

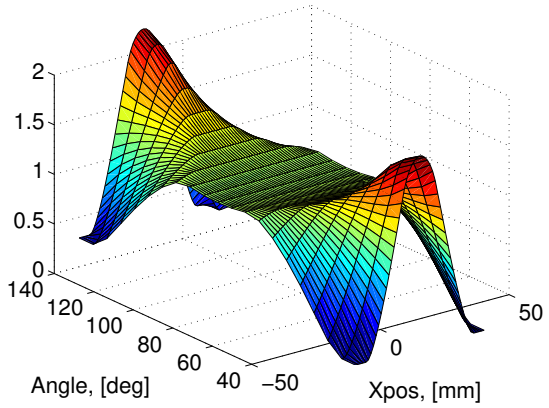


(b) Correction on defocusing for 25 mm spherical mirror and 20x40 mm grating size as function as grating position

Script Grating_correction.m

## Mirror acceptance

Cross-section of two circles (detector and focus point of abbe diffraction limit).

Focus spot is circle with radius defined by Abbe difraction limit. Detector diameter is fixed and equal 2 mm and supposed to be exactly in focus of 25mm with 50.8 focus length OAP mirror.

Also was taken into account, that frequency of SPR depent from observation angle, so at different angle we have different spot size. Script OverlapCorrections.m